Temperature-Dependent Ion Migration Underlies Sequence-Specific RNA Collapse

Heyang Zhang, Hiranmay Maity, and Hung T. Nguyen*

Department of Chemistry, State University of New York at Buffalo, Buffalo, New York 14260-3000, United States

E-mail: nguyenh@buffalo.edu

Abstract

Ions and temperature jointly regulate RNA structure, dynamics and phase behavior, yet their coupled effects remain poorly understood at the molecular level. Single-stranded RNA (ssRNA), a ubiquitous and functionally versatile class of RNA, presents a particularly challenging target due to its intrinsic flexibility and pronounced sensitivity to ionic and thermal perturbations. Here, we develop and apply coarse-grained simulations incorporating a temperature-dependent Mg^{2+}-phosphate potential to elucidate how electrostatics, stacking, and hydration collectively determine ssRNA behavior. Our simulations quantitatively reproduce experimental SAXS profiles across a broad range of ionic conditions and reveal a non-monotonic temperature dependence of RNA compaction: ssRNAs expand upon heating, reach a sequence-specific maximum size, and then collapse as enhanced counterion condensation dominates. Rising temperature strengthens ion-RNA interactions, leading to a reorganization from diffusive to inner-sphere coordination, directly linking RNA collapse to ion dehydration. Our results establish that the ion atmosphere is a dynamic, sequence-encoded extension of RNA structure. This framework provides molecular insight into how tempera-

ture and ions govern RNA conformational transitions, offering a microscopic basis for RNA thermoadaptation, cold-induced misfolding, and RNA phase transitions.

Graphical Abstract

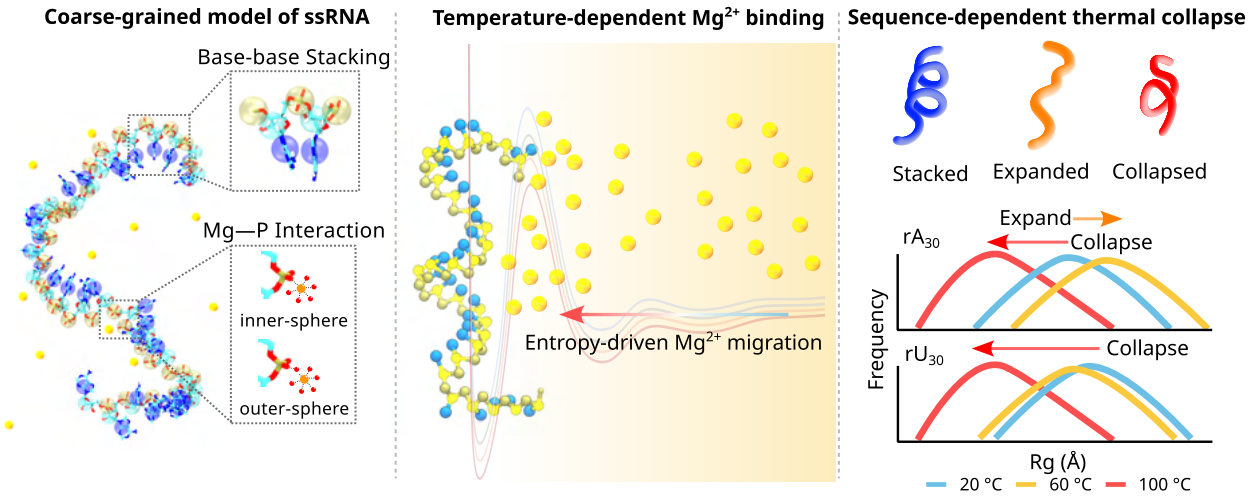

Introduction

RNA plays a central role in virtually all biological processes, with its function intricately linked to its structure.[1–7] The structural landscape of RNA is highly dynamic and shaped by a wide range of intrinsic and extrinsic factors,[8] including the primary sequence,[9] physiological conditions,[7] ion concentrations,[10–14] molecular interactions with other RNAs and proteins,[15,16] as well as covalent RNA modifications.[17–20] Among its diverse structural motifs, single-stranded RNA (ssRNA) is particularly versatile. Beyond serving as linkers between structured regions, ssRNA contributes to higher-order RNA architecture and functions as regulatory elements throughout the mRNA lifecycle.[21–26] A wide array of cellular proteins, including those that are highly expressed, exhibit selective affinity for ssRNA, mediating essential steps in gene expression at both the transcriptional and post-transcriptional levels.[27–31]

The interactions between ssRNAs and regulatory proteins are expected to be dependent on sequence-specific structures. However, the molecular mechanisms underlying many processes involving ssRNAs remain poorly understood, primarily due to the limited understanding of their structural features. This challenge has persisted since the pioneering studies of the late 1950s.[32] Early experimental techniques provided the fundamental insights for both intrinsic and extrinsic factors influencing the single-stranded helices of poly(rA), poly(rU), and poly(rC).[33–43] In contrast, poly(rG) readily self-associates into higher-order structures, most notably the G-quadruplex.[44] These studies identified base stacking as a dominant energetic determinant of helix formation, with temperature and ion concentration significantly impacting the helix formation kinetics.[45] Subsequent experimental advances have highlighted the substantial effects of Mg^{2+} on the structures of ssRNA.[46–49] More recently, with growing interest in understanding biomolecular condensates, ssRNA has been shown to interact with arginine/glycine-rich intrinsically disorder regions, impacting the viscoelastic and dynamic properties of these condensates.[50–54] Short poly(rA) sequences form Mg^{2+}-dependent condensates, yet the structural organization of ssRNA within these assemblies remains largely

unknown.[55]

In principle, atomistic MD simulations can be used to probe ssRNA conformational ensembles, but their accuracy remains limited by imperfect force fields, which often lead to unrealistic collapse and inadequate treatment of ion effects.[56–63] Coarse-grained (CG) models provide a more computationally efficient alternative, although most have focused on well-folded sequences.[64–68] Several recent CG approaches tend to overestimate ssRNA size, likely due to oversimplified base-stacking representations, and rely on *ad hoc* treatments of ion-RNA interactions.[69–71] We recently extended our Single-Interaction-Site (SIS) model[72] by incorporating explicit Mg^{2+}-RNA interactions, revealing the extension of ssRNA ion atmosphere.[73] However, the SIS model, in its current form, cannot realistically account for base-stacking, thus failing to model the sequence effects on ssRNA structural ensemble.

To overcome these limitations, we resorted to the Three-Interaction-Sites (TIS) representation of RNA, where each nucleotide is modeled by three CG beads corresponding to the ribose, phosphate, and nucleobase groups (Fig. 1A).[65] Compared to our earlier model,[74] which occasionally suffered from numerical instabilities in evaluating the dihedral component of the stacking potential, the present implementation introduces revised functional forms and an optimized parameter set (details provided in "Materials and Methods" and "Supporting Information", SI). These refinements improve numerical stability and yield a more accurate balance among base stacking, backbone flexibility, and electrostatic interactions. A key advance in this work is the explicit treatment of divalent ion-phosphate interactions using temperature-dependent potentials of mean force (PMFs) derived from the liquid-state integral equation theory.[75–77] The resulting PMFs naturally capture both inner- and outer-sphere coordination of Mg^{2+} with RNA (Fig. 1B), while monovalent ions are treated implicitly through a mean-field Debye–Huckel term.

Using unbiased CG simulations, we find excellent agreement between the predicted ssRNA conformational ensembles and experimental small-angle X-ray scattering (SAXS) data,[49] capturing transient helical structures populated by rA_{30} due to its stable base-

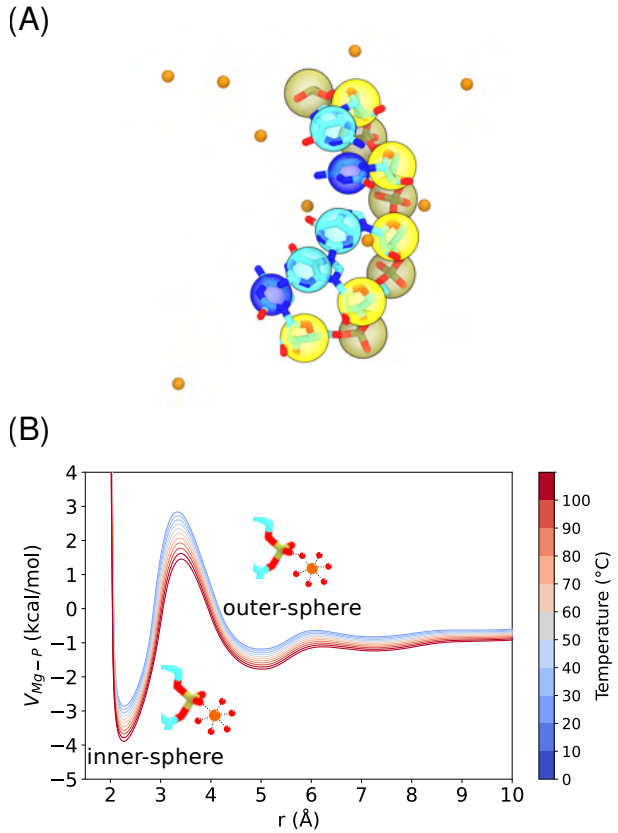

Figure 1: **(A)** Three-interaction-site (TIS) representation of RNA, with beads for ribose, phosphate, base, and explicit Mg^{2+} ions. **(B)** Temperature-dependent potential of mean force (PMF) between Mg^{2+} and phosphate, obtained from 1D-RISM, capturing both inner-sphere and outer-sphere coordination as a function of temperature.

stacking interactions. Subtle sequence-dependent differences in stacking propensity give rise to distinct local ionic environment, underscoring the tight coupling between RNA structural organization and its surrounding ion atmosphere. More importantly, we revealed a pronounced temperature dependence of ssRNA conformations and ion distributions. As temperature increases, RNA undergoes a non-monotonic transition, first expanding and subsequently collapsing, due to the interplay between base unstacking and temperature-enhanced ion-mediated attractions. Strikingly, we observed a reorganization of the ion atmosphere at elevated temperatures in which diffuse ions condense inward to form direct contacts with the phosphate backbone, leading to the partial collapse of the extended ion cloud. Together, these findings establish a robust computational framework for probing the structural and

electrostatic features of RNA under varying ionic and thermal conditions. This approach provides a foundation for investigating how RNA behavior and ion distributions are reshaped in dense, phase-separated environments and at their interfaces. It will also enable studying of broader temperature-responsive phenomena, including cold-induced misfolding and RNA thermometers that control gene expression through structural transitions.

Materials and Methods

Temperature-Dependent Ion-Phosphate Interaction. Following our previous procedure,[74] we resort to the well-known Reference Interaction Site Model (RISM) theory to calculate the potential of mean force (PMF) between Mg^{2+} and phosphate. We use 1D-RISM[75,76,78] to calculate the radial distribution function $g_{Mg-P}(r)$, and then convert it to PMF: $W(r) = -k_B T \ln g_{Mg-P}(r)$. The theory starts with the Ornstein–Zernike (OZ) equation:

$$h(r_{12}) = c(r_{12}) + \rho \int dr_3 c(r_{13}) h(r_{32}), \tag{1}$$

where r_{ij} is the distance between particles i and j, c is the direct correlation function, and h (the total correlation function) is related to g as $h(r_{ij}) = g(r_{ij}) - 1$. To solve the OZ equation, another equation (known as the closure relation) connects h and c:

$$g(r_{12}) = \exp[-\beta u(r_{12}) + h(r_{12}) - c(r_{12}) + b(r_{12})], \tag{2}$$

where u_{ij} is the pairwise potential energy function and b_{ij} is an unknown "bridge function". In our work, we choose to use the partial series expansion of order-n (PSE-n) closure[79] to improve the results for highly charged systems (compared to Kovalenko–Hirata closure[80]), while

circumventing the convergence issues associated with the hypernetted-chain closure:[78,81,82]

$$g = \begin{cases} \exp(-\beta u + h - c) & \text{if } g \leq 1 \\ \sum_{k=0}^{n} \frac{(-\beta u + h - c)^k}{k!} & \text{if } g > 1 \end{cases}. \tag{3}$$

In the above equation, all r_{12} are removed for brevity. The RISM equations are solved iteratively using the 1D-RISM code implemented in Amber[77] until obtaining converged results. The theory requires the dielectric constant, bulk concentrations and topologies (bond lengths and bond angles) of every species in the system as well as the pairwise interaction potentials $u(r)$ for every pairs. In our case, the system is comprised of Mg^{2+}, phosphate and water. The concentration of MgP_2 is set to 1 mM. We used a 1D grid with a grid spacing of 0.025 Å and 131,072 grid points. Parameters for Mg^{2+} were taken from the Amber force field. We used the cSPC/E model for water, which introduces van der Waals terms for the hydrogen atoms of the SPC/E water to prevent them to collapse in RISM. For phosphate, we used a single-site representation to overcome the convergence problems in RISM as in our previous work.[74] We then iteratively solved the RISM equations using the PSE-3 closure to a residual tolerance of 10^{-12} at different temperatures. g_{Mg-P} is one of the direct output, from which we obtain $W(r) = -k_B T \ln g_{Mg-P}(r)$.

Three-interaction-site (TIS) RNA model with explicit Mg^{2+}. TIS model represents each nucleotide with three spherical beads (interaction sites), corresponding to the phosphate, ribose and nucleobase.[83] The beads are positioned at the center-of-mass (COM) of the chemical groups (Fig. 1A). Overall, the energy function describing the interactions between the beads is expressed as a sum of contributions from the bond length (U_{BL}), bond angle (U_{BA}), single-stranded stacking (U_{ST}), hydrogen bonding (U_{HB}), excluded volume (U_{EV}), and electrostatic (U_{EL}) interactions:

$$U_{TIS} = U_{BL} + U_{BA} + U_{ST} + U_{HB} + U_{EV} + U_{EL}. \tag{4}$$

We use the harmonic approximation for U_{BL} and U_{BA}, where the equilibrium values (k_b, k_θ, r_0, and θ_0) are listed in Tables S1 and S2. Excluded volume interactions are modeled using the Weeks–Chandler–Andersen (WCA) potential:[84]

$$U_{EV} = \begin{cases} \varepsilon_0 \left[\left(\frac{D_0}{r}\right)^{12} - 2\left(\frac{D_0}{r}\right)^{6} + 1 \right], & r \leq D_0 \\ 0, & r > D_0 \end{cases}, \tag{5}$$

where $\varepsilon_0 = 1$ kcal/mol and $D_0 = R_i + R_j$. R_i for ions and RNA beads are listed in Table S3. The WCA term vanishes if the interacting sites are separated by a distance greater than D_0. For interactions between two bases, we set $D_0 = 3.2$ Å to favor stacking.

Stacking potential. Stacking interactions U_{ST} are applied to any two consecutive nucleotides along the chain:

$$U_{ST} = \frac{U_{ST}^0}{1 + k_r(r - r_0)^2 + k_\phi(|\phi_1 - \phi_{1,0} - \pi| - \pi)^2 + k_\phi(|\phi_2 - \phi_{2,0} + \pi| - \pi)^2}, \tag{6}$$

where r is the distance between B_i and B_{i+1}, $\phi_1(P_i, S_i, P_{i+1}, S_{i+1})$ and $\phi_2(P_{i+2}, S_{i+1}, P_{i+1}, S_i)$ are dihedral angles around the sugar-phosphate bonds (Fig. S2A). This functional form is implemented in OpenMM to make sure dihedral angles are continuously wrapped around $-\pi$ and π, while keeping a single minimum at the equilibrium value (Fig. S1). All equilibrium values (r_0, $\phi_{1,0}$, and $\phi_{2,0}$) match the A-form RNA helix.[83] We recalibrated U_{ST}^0 for all 16 pairs of dinucleotides to accurately reproduce thermodynamics of stacking derived from the nearest neighbor model (Fig. S2B).[83,85] The calibration procedure and U_{ST}^0 values are reported in SI and Table S4.

Electrostatic interactions. To model explicit Mg^{2+} while keeping monovalent ions implicit, we use our previously established liquid-integral theory.[74] Briefly, the screening effect of the ionic buffer is approximated using Debye–Huckel (DH) equation. This accounts for the

electrostatic repulsions between P–P and Mg–Mg:

$$U_{DH}(r) = \frac{l_B}{2} k_B T \sum_{i,j} \frac{Q_i Q_j \exp(-\frac{r_{ij}}{\lambda})}{r_{ij}}, \tag{7}$$

where $\lambda = (8\pi l_B \rho_1)^{-1/2}$ is the DH screening length determined by the number densities of monovalent ions, ρ_1. The Bjerrum length $l_B = \frac{e^2}{4\pi\epsilon_0\epsilon_r k_B T}$ sets the strength of the interactions, where e is the elementary charge, ϵ_0 is the vacuum permittivity, and ϵ_r is the temperature-dependent dielectric constant of water. The effective charge of phosphate, $Q_P(T, C_1, C_2)$, depends on concentrations of both the monovalent (C_1) and divalent ions (C_2) using counterion condensation theory.[86–88] The effective potential between P–Mg^{2+} is subsequently calculated as following:

$$V_{Mg-P}(r) = W(r) + [U_{DH}(r) - W(r)] \exp\left(-\frac{a^2}{r^2}\right), \tag{8}$$

where $W(r)$ is the RISM PMF which dominates at short distance, and $U_{DH}(r)$ is the DH potential (Eq. 7) which is predominant at large separation. We set $a = 5$ Å as in our previous work.

Langevin dynamics simulations. All simulations are performed using OpenMM 8.0.0[89] on NVIDIA A100 Graphics Processing Unit (GPU). We use LangevinMiddleIntegrator in OpenMM to integrate the equations of motion in NVT ensemble with a timestep of 2 fs. Mg^{2+} ions were initially placed at random positions within a cubic box containing the ssRNA of interest. The box size ranges from 420 Å to 720 Å, depending on the bulk Mg^{2+} concentrations, and is chosen such that at least 200 Mg^{2+} ions are present. We apply periodic boundary conditions in all three dimensions to minimize finite-size effects. We use low-friction Langevin dynamics to enhance conformational sampling, with a friction coefficient of 0.01 ps^{-1}. Snapshots are saved every 10,000 integration steps, and all trajectories are examined for equilibration and convergence before analyses.

Analyses. *Calculations of Mg^{2+} preferential interaction coefficient.* First, all frames are

aligned to the ssRNA COM. The local concentration of Mg^{2+} is subsequently computed as:

$$C_{Mg}(r) = \frac{N_{Mg}(r)}{\Delta V_r C_{Mg}}, \tag{9}$$

where $N_{Mg}(r)$ is the number of Mg^{2+} ions within the spherical shell of volume ΔV_r between r and $r + \Delta r$, and C_{Mg} is the initial Mg^{2+} concentration ($C_{Mg} = \frac{N}{V_S}$, where N is the total number of Mg^{2+} and V_S is the volume of the simulation box). Because ssRNA is highly negatively charged, Mg^{2+} are attracted to phosphate groups, thus the effective bulk concentration, C_{Mg}^{eff}, is lower than the initial value. We determine C_{Mg}^{eff} as the plateau value in the concentration profile $C_{Mg}(r)$ at large separation (Figs. S33, S34, and S35).

The preferential interaction coefficient (Γ_{Mg}) reports the excess number of ions associated with RNA relative to bulk solution.[90,91] We calculate Γ_{Mg} using the Kirkwood–Buff integral:

$$\Gamma_{Mg} = C_{Mg}^{eff} 4\pi \int_{r=0}^{r_{cs}} [g(r) - 1] r^2 dr, \tag{10}$$

where $r_{cs} = \frac{L}{2}$ is half the simulation box length, and r is the distance from Mg^{2+} to the RNA COM.

Partitioning of inner-sphere, outer-sphere, and diffusive ion. A Mg^{2+} ion is classified as inner-sphere if the Mg-phosphate distance falls within the first peak of $g_{Mg-P}(r)$ ($r < 3.2$ Å). Mg^{2+} within the second peak (3.2 Å $< g_{Mg-P}(r) < 6.0$ Å) is assigned to the outer-sphere population. The number of diffuse ions is then computed as $N_{dif} = \Gamma_{\mathrm{Mg}} - N_{inner} - N_{outer}$. To compare between two independent groups (e.g. inner-sphere Mg^{2+} counts between rA_{30} and rU_{30} at a given temperature), the Welch's two-sided t-test is used, which does not assume equal variance between groups. For each group, the mean and standard deviation are reported.

Calculations of SAXS Profiles from Coarse-Grained Trajectories. We first backmap 10,000 randomly selected conformations to all-atom representations using Arena.[92] Because Arena only recognizes standard RNA atom names, we map the phosphate, sugar, and base

beads in the CG model to P, C2', and C4 atoms, respectively. To remove steric clashes after this procedure, each structure is subjected to an energy minimization using Amber bsc0 force field with $\chi OL3$ corrections.[56,93] The structural deviation between pre- and post-minimization conformations is below SAXS detection threshold (RMSD = 3.8 Å; Fig. S3A). We then calculate SAXS profiles under the same conditions in experiments using CRYSOL with default parameters.[94]

Ion atmosphere 2D projection. Direct superposition of instantaneous ion distributions from successive trajectory snapshots provides a qualitative view of the ion atmosphere surrounding structured RNAs. However, for flexible ssRNA, such averaging leads to severe blurring that obscures spatial features of ion localization.[95] To generate an interpretable representation of the Mg^{2+} ion atmosphere, we first remove the translational and rotational motions of ssRNA by aligning each frame to the ssRNA COM and principle axes. We project the distance from every Mg^{2+} ion to its closest phosphate group using the following procedure. We define r_z as the axial distance along the RNA first principal axis, and r_{xy} is the in-plane (lateral) distance. The azimuthal angle is determined as $\theta = \arctan\frac{r_y}{r_x}$, where x and y are the components of the Mg–P vector in the xy-plane. To preserve directional information in the 2D projection, the sign of the lateral displacement is assigned according to the sign of θ, resulting in the directional in-plane distance: $r^{min}_{\mathrm{Mg^{2+}-P_{xy}}} = \mathrm{sgn}(\theta) \cdot \sqrt{x^2 + y^2}$ (Fig. 3C).

Calculations of solvent-accessible surface area (SASA). SASA is calculated using the FreeSASA Python package.[96] In this method, a spherical probe representing the solvent molecule rolls over the solute molecule. We use the classical Lee–Richards algorithm,[97] in which the surface area is approximated by the contour of successive slices. We set the probe radius to 2.0 Å to approximate the size of a hydrated Mg^{2+} ion. The total SASA can be decomposed into contributions from the phosphate, sugar, and nucleobase groups.

Calculations of the orientational correlation function. The orientational correlation func-

tion (OCF) is defined as:

$$OCF = \langle \cos\theta_{ij} \rangle = \langle r_i \cdot r_j \rangle, \tag{11}$$

where r_i is the normalized bond vector connecting the ith and $(i+1)^{th}$ phosphate groups. The OCF is evaluated as a function of sequence separation $|i-j|$, which measures the correlation between local backbone orientations over increasing contour distances. The resulting OCF is averaged over all conformations in the structural ensemble to characterize the mean chain stiffness and directional persistence of ssRNA.

Clustering of conformational ensembles. Feature tables of rA_{30} at 5 mM Mg^{2+} and 20 mM Na^{+} are generated at 0 °C, 40 °C, 80 °C, and 100 °C, each containing SASA, R_g, end-to-end distance, stacking energy, and Mg–phosphate interaction energy. The datasets are concatenated and robustly scaled (5 to 95% quantile range) prior to dimensionality reduction. We apply t-distributed stochastic neighbor embedding[98] (t-SNE) using Euclidean distance and sweep perplexity values (30 to 300) to balance local and global structure preservation. The resulting 2D embeddings are then clustered using HDBSCAN[99] with varying minimum cluster size (100 to 400). To identify optimal hyperparameters, we compute Silhouette scores in both the high-dimensional feature space and the 2D embedding, taking their product as a combined metric.[100] The best-scoring settings are finally used for clustering and visualization of temperature-dependent population shifts (Fig. S10).

Results and Discussion

Distinct Structural Ensembles of rA_{30} and rU_{30}. To access the model's accuracy in capturing ssRNA structural ensembles, we compare the simulated radii of gyration (R_g) and SAXS profiles with experiment for rA_{30} and rU_{30} at 20 °C. Across wide concentrations of both Mg^{2+} and monovalent ions, R_g values agree well with SAXS-derived measurements, capturing ion-induced compaction (Figs. 2A, S8 and Table S5).[49,101] We observe that rA_{30} has smaller R_g than rU_{30} across all salt concentrations due to stronger adenine stacking, which agrees

with experimental data. The computed SAXS profiles are in quantitative agreement with experiments (Fig. S5), and Kratky plots further highlight sequence-dependent differences in structural ensemble and compaction upon addition of Mg^{2+}. Both RNAs remain largely unstructured across the tested ion conditions (Fig. 2B); however, at 5 mM Mg^{2+}, the Kratky curve of rA_{30} bends downward, suggesting the formation of partially folded, compact conformations (Figs. S6 and S7).

To directly probe the ssRNA structures, we compute the OCF between phosphate groups (Fig. 2C). Changes in backbone direction reduce the OCF, which becomes negative when the vectors approach an antiparallel orientation. For rA_{30}, OCFs exhibit oscillatory behavior across ionic conditions. With added Mg^{2+}, the correlation decays rapidly, changing from positive to negative values, strongly suggesting a signature of helical structures. In contrast, rU_{30} shows monotonic decay under 20 mM Na^{+} and 1 mM Mg^{2+}. Above 1 mM Mg^{2+}, transient secondary structures emerge, reflected by a weaker oscillatory curve compared to rA_{30}. These results are consistent with previous reconstruction of structural ensembles from SAXS for homopolymeric ssRNA.[49]

Stacking Interactions Dictate Helical Formation. To elucidate the difference in helical propensity between the two sequences, we calculate the 2D distributions of SASA and stacking propensity, defined as the fraction of nucleobases in stacked conformations (results for 20 mM Na^{+} + 5 mM Mg^{2+} shown in Fig. 2D). The two distributions of rA_{30} and rU_{30} are well separated, highlighting distinct conformational ensembles. rA_{30} transiently adopts a right-handed single-stranded helix with a maximum contiguous stacking length (N_{stack}^{max}) of 9 $\pm$ 4 nucleotides, whereas rU_{30} exhibits shorter stacked segments (N_{stack}^{max} of 6 $\pm$ 2) (Fig. 2E, top). As a result, the coil (unstacked) regions are shorter for rA_{30} (5 $\pm$ 2 nucleotides) than for rU_{30} (7 $\pm$ 3 nucleotides), consistent with stronger base stacking in the former (Fig. 2E, bottom). Because stacking interactions occur primarily between nearest neighbors, such helicity is expected to be only weakly cooperative.[102,103] Our results are consistent with single-molecule force experiments that revealed alternating helical and

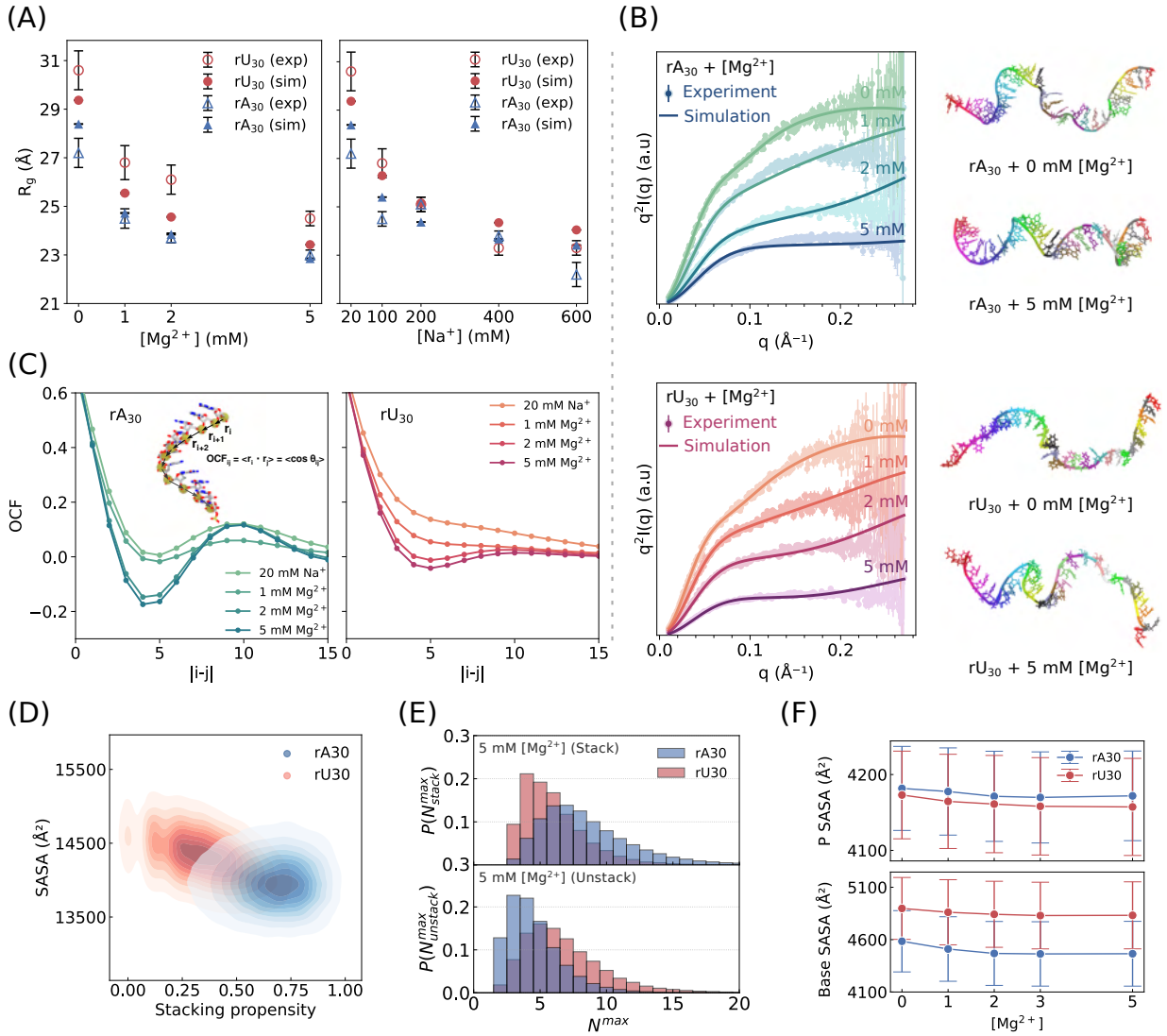

Figure 2: rA_{30} and rU_{30} populate distinct structural ensembles. **(A)** Radii of gyration from simulation plotted against SAXS-derived values for rA_{30} (blue) and rU_{30} (red) under varying Mg^{2+} and Na^{+} concentrations, showing sequence- and ion-dependent compaction. **(B)** Comparison between simulated SAXS profiles with experiments for rA_{30} (top) and rU_{30} (bottom). On the right shown representative conformations obtained by all-atom backmapping from coarse-grained coordinates. **(C)** Orientation correlation functions for rA_{30} (left) and rU_{30} (right) at various ion concentrations. **(D)** Solvent-accessible surface area *vs.* stacking propensity distribution of rA_{30} and rU_{30} in 5 mM Mg^{2+}. **(E)** Distribution of maximum consecutive stacking (top) and unstacking (bottom) in 20 mM Na^{+} + 5 mM Mg^{2+}. **(F)** Decomposing solvent-accessible surface area to phosphate (top) and base (bottom) contributions. Error bars are standard deviations.

coil regions for poly(rA), but not for poly(rU).[104] It is also supported by crystallographic analyses of the ApApA trimer demonstrating intrinsic helical order in poly(rA).[105] Our simulations therefore support a block copolymer picture of ssRNA, in which stacked and unstacked domains coexist. We anticipate that the differences in stacking translate directly into changes in SASA, especially around the nucleobases. While the phosphate SASA is similar between the two sequences, the nucleobase SASA is much smaller for rA_{30} (Fig. 2F), even though adenine is larger than uracil. This indicates that stronger stacking buries nucleobases and reduces their solvent accessibility. Such modulation of solvent exposure may in turn influence local ion interactions and potentially modulate the recognition of single-stranded regions by regulatory proteins.[106,107]

Structure-Dependent Ion Atmosphere. The degree of ion binding to RNA can be quantified using the preferential interaction coefficient Γ_{Mg}, which reports the excess number of ions associated with RNA relative to bulk solution.[90,91,108] Consistent with ion counting experiments,[49] our simulations reproduce the overall magnitude of Γ_{Mg} (Fig. 3A, Table S6). Experimentally, rA_{30} attracts approximately 1.5 more Mg^{2+} ions per chain than rU_{30} over the range of 0-3 mM Mg^{2+} and 20 mM Na^{+}, corresponding to a lower competition coefficient ($M_{1/2} = 0.9 \pm 0.1$ mM for rA_{30} vs. 1.3 ± 0.3 mM for rU_{30}). Although these values overlap within experimental uncertainty, their mean difference implies that nearly 40% higher bulk Mg^{2+} concentration is required to displace half of the monovalent ions surrounding rU_{30}.[49] This subtle sequence dependence is not captured by our simulations. However, prior work on ssDNA also found identical Γ_{Mg} for dA_{30} and dT_{30} despite pronounced differences in stacking propensity.[48,109]

To further probe the ion atmosphere in a greater detail, we partition the Mg^{2+} binding into inner-sphere (direct phosphate coordination), outer-sphere (water-mediated interaction), and diffusive regions (Fig. 3B).[73,110] The Welch's t-test uncovers small but statistically significant differences between various RNA sequences. rU_{30} binds more inner-sphere Mg^{2+} (3.4 ± 1.6 per chain) than rA_{30} (3.1 ± 1.6 per chain) with $p < 0.001$. In contrast, rA_{30}

recruits slightly more outer-sphere (2.8 ± 1.5 *vs.* 2.6 ± 1.4, $p < 0.001$) and diffusive Mg^{2+} (4.9 ± 1.6 *vs.* 4.8 ± 1.6, $p < 0.001$) (Fig. 3B). Thus, the overall ion atmosphere of rU_{30} is slightly more compact than the rA_{30} counterpart. In all ssRNAs, the majority of ions remain in the diffusive regime, consistent with our previous report that unstructured RNAs favor diffuse, weakly localized ionic environments.[73]

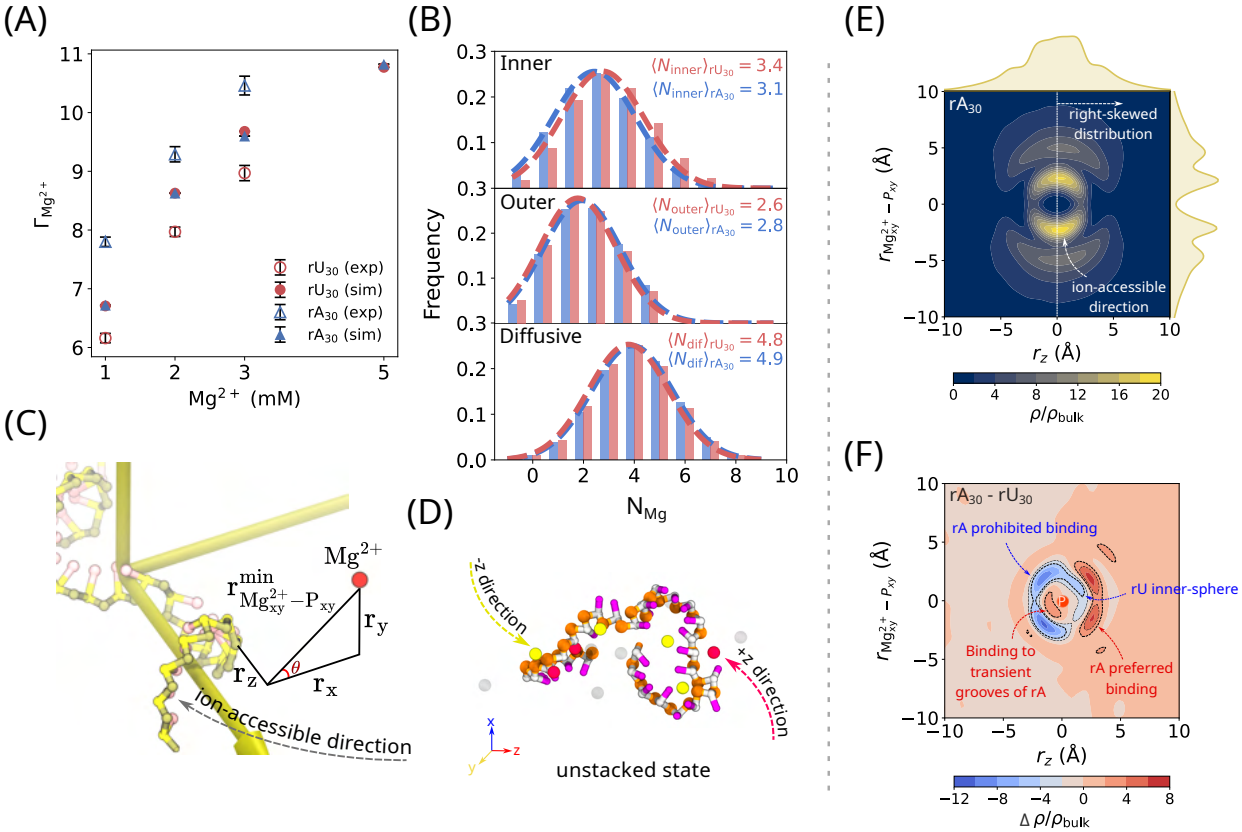

Figure 3: Sequence- and structure-dependent ion atmosphere. **(A)** Excess Mg^{2+} per chain for rA_{30} (blue) and rU_{30} (red) from simulations and buffer exchange-atomic emission spectroscopy.[49] **(B)** Partitioning of Mg^{2+} into inner-sphere (top), outer-sphere (middle), and diffusive (bottom) binding modes. **(C)** Schematic of the alignment for ion projection, where the RNA major axis is along the z-axis. Distances $r^{min}_{Mg^{2+}-P_{xy}}$ and r_z are Mg^{2+}–phosphate separation in the xy- and z-directions, respectively; θ is the azimuthal angle. In the right-handed helical state, Mg^{2+} accessibility is restricted from a certain direction due to the presence of the sugar and base. **(D)** Schematic of the unstacked state, where Mg^{2+} can approach from both directions along the z-axis. **(E)** 2D density map of Mg^{2+} around rA_{30}, showing a right-skewed distribution consistent with the transient helical structures. The ion-accessible direction corresponds to the most populated region. **(F)** Difference density map between rA_{30} and rU_{30}. Red regions highlight preferred Mg^{2+} binding for rA_{30} in the positive z-direction and transient groove binding near the phosphate, whereas blue regions are sites more accessible in rU_{30}.

To visualize sequence-dependent ion binding patterns, we aligned the RNA COM and principle axes, thus removing the RNA translational and rotational movement. Subsequently,

we project the distance between every Mg^{2+} and its closest phosphate group onto a 2D surface (see Materials and Methods). Since rA_{30} has a small preference for helical structures, stacked phosphates align along the positive z-axis from 5' to 3', establishing a preferred direction of ion approach toward the backbone (Fig. 3C). In contrast, in the unstacked state, phosphates are disordered, allowing ions to approach from both the +z and -z directions (Fig. 3D). The resulting 2D density map of rA_{30} shows a slightly right-skewed distribution along the z-axis, consistent with the anisotropic ion localization expected for a transient helical structure (Figs. 3E, S16A). Additional insights emerge by subtracting the rU_{30}'s distribution from rA_{30}'s (Figs. 3F, S16B): a distinct region of enhanced Mg^{2+} density appears along the positive z-axis, indicating a site where rA_{30} preferentially binds ions. Conversely, the region in the corresponding negative z-axis is depleted for rA_{30}, suggesting that this binding site is more accessible in rU_{30}. Furthermore, localized hotspots of density indicate Mg^{2+} association with the transient helical grooves of rA_{30}, reflecting its stacked, groove-forming structure that is absent in the largely unstacked rU_{30} ensemble. In other words, the chirality of the RNA imposes a chiral organization on its counterions. This phenomenon is analogous to how water molecules form a chiral hydration structure around duplex DNA, aligning in helical patterns along the major and minor grooves of the double helix.[111–114] Together, these results demonstrate that Mg^{2+} ions neutralize ssRNA by organizing to form a complicated ion atmosphere shaped by the RNA's 3D organization. The ion atmosphere is therefore an extension of the RNA's structure, inheriting its helical grooves, directional geometry, and chirality rather than forming a uniform shell.[115] Such coupling between RNA shape and ion distribution underscores that ions "sense" the helix's handedness and stabilize the structure in an asymmetric fashion, which has important implications for RNA folding and molecular recognition.

Thermal Compaction of ssRNA. To model Mg^{2+}-RNA interactions at different temperatures, we employ our previously developed framework where the RISM theory is used to calculate the PMF between Mg^{2+}-phosphate $W(r) = -k_B T \ln g(r)$.[74] Temperature af-

fects the ion binding through two coupled terms: (i) the inverse thermal factor $\beta = 1/k_B T$, and (ii) the dielectric constant of water, $\epsilon_r(T)$, which decreases at elevated temperature and thereby effectively strengthens electrostatic attractions. Together, those effects stabilize both inner- and outer-sphere minima of the Mg^{2+}–phosphate PMF at elevated temperatures (Fig. 1B). This framework is consistent with counterion condensation theory: Mg^{2+} binding to phosphate is accompanied by the release of ordered water and competing counterions, yielding a net favorable entropy change that stabilizes both inner- and outer-sphere Mg^{2+} at high temperatures.[87] In particular, the temperature dependence in dielectric constant of water gives rise to a substantial entropic contribution in the electrostatic interaction.[116]

Remarkably, we found that R_g values of ssRNAs display non-monotonic behaviors when the temperature rises from 0 °C to 100 °C (Fig. 4B). Even in the absence of Mg^{2+}, rA_{30} exhibits a relatively long expansion phase, reaching a maximum at $T_{max} = 76$ °C before undergoing mild collapse, whereas rU_{30} shows limited expansion and collapses earlier at $T_{max} = 48$ °C. Introduction of 1 mM Mg^{2+} sharply lowers T_{max} (to 59 °C for rA_{30} and 15 °C for rU_{30}), with little additional shift up to 5 mM.

We rationalize this non-monotonic behavior by considering the coupled effects of electrostatics and base stacking. The Bjerrum length $l_B = \frac{e^2}{4\pi\epsilon_0\epsilon_r(T)k_B T}$ (where e is the elementary charge and ϵ_r (T) is the temperature-dependent dielectric constant of water) sets the strength of electrostatic interactions. With increasing temperature, the dielectric constant decreases more rapidly ($\epsilon_r T$ decreases), resulting to an overall lengthening of l_B (Fig. S11A). Consequently, electrostatic interactions become stronger at higher temperatures, promoting enhanced counterion condensation on the phosphate backbone (Fig. S11B). The resulting effective P–P repulsion thus exhibits a non-monotonic temperature dependence: it initially increases as the electrostatic interactions strengthen but subsequently weakens once extensive counterion adsorption more effectively neutralizes the backbone charges (Fig. S11D). Additionally, base-base stacking further modulates this behavior in a sequence-dependent manner. Stacking propensity decreases monotonically with temperature (Fig. 4E), so the

thermal disruption of stacking interactions drives an initial expansion of the RNA. The overall temperature profile of R_g therefore reflects a balance between stacking and electrostatic effects: R_g first increases as stacking weakens, then subsequently decreases as counterion condensation dominates at higher temperatures. Adenines stack more favorably than uracils, explaining why rA_{30} expands substantially upon heating, whereas rU_{30} (with weak stacking, $< 50\%$ at 0 °C) shows minimal expansion. Interestingly, Mg^{2+} affects stacking interactions minimally (Fig. S12). Therefore, the pronounced dependence of T_{max} on Mg^{2+} arises mainly because divalent cations are far more effective at neutralizing RNA charge than monovalent ions, altering the electrostatic balance that governs the transition. This mechanism also explains the observed saturation at high Mg^{2+} concentrations.

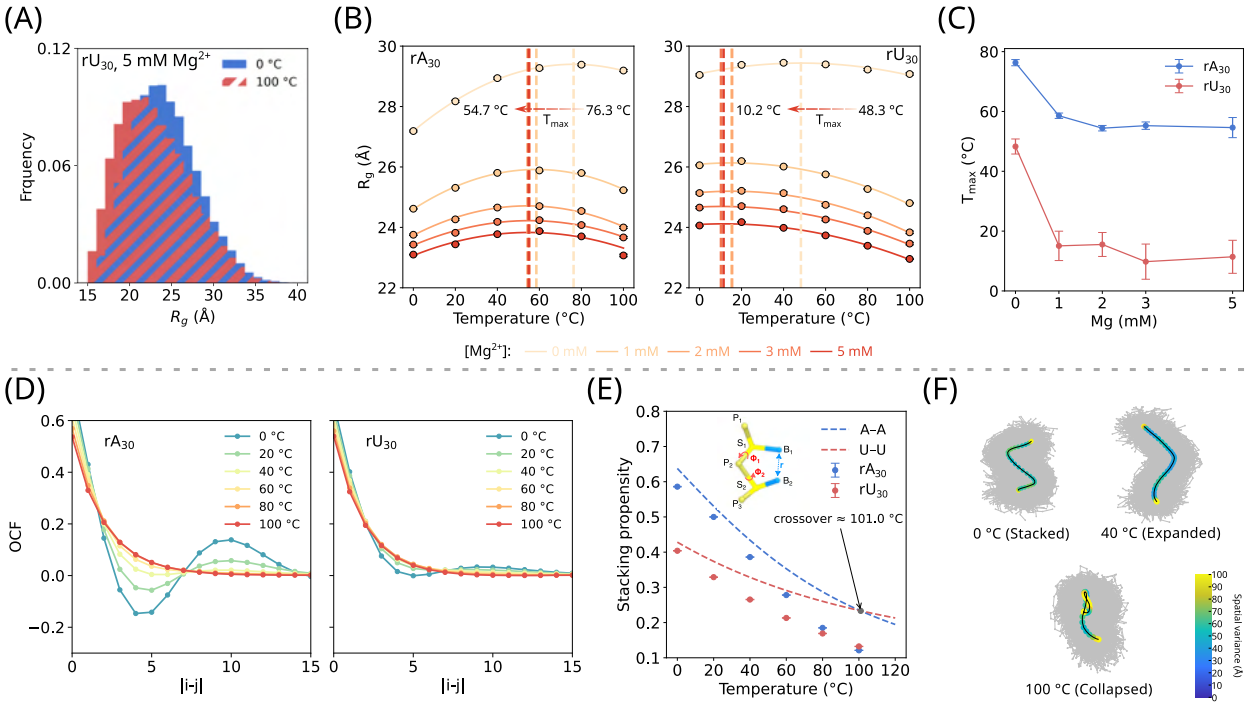

Figure 4: ssRNA collapses at high temperature. **(A)** Distribution of R_g at 0 °C (blue) and 100 °C (red) of rU_{30} in 5 mM Mg^{2+}. **(B)** R_g of rA_{30} (left) and rU_{30} (right) as a function of temperature in 0-5 mM Mg^{2+}. Vertical dashed lines denote T_{max}, the temperature of maximal expansion, which marks the transition from chain expansion to collapse. **(C)** Dependence of T_{max} on Mg^{2+} concentration for rA_{30} (blue) and rU_{30} (red). **(D)** Orientational correlation functions from 0 °C to 100 °C for rA_{30} (left) and rU_{30} (right). **(E)** Stacking propensity decreases with temperature for rA_{30} and rU_{30}. Dotted lines show prediction from the dinucleotide model, which underestimates the accelerated decay observed in long sequences. **(F)** Representative conformational ensemble of rA_{30} at 0 °C, 40 °C, and 100 °C.

To dissect the conformational ensembles of ssRNAs across temperatures, we examined the 2D distribution of SASA and stacking propensity at various ionic conditions. As temperature rises, all RNAs exhibit a shift towards lower stacking propensity and higher SASA. This shift occurs more rapidly for rA_{30} than for rU_{30} (Fig. S9). Consistently, projection of the higher-dimensional space comprising of R_g, end-to-end distance, SASA, stacking potential energy, and Mg–P interaction energy onto two dimensions using t-SNE revealed the same trend (Fig. S10). For rA_{30}, pronounced helical signatures are evident at 0 °C and 20 °C, characterized by oscillatory OCFs that alternate between negative and positive values. These helical correlations vanish at high temperatures, indicating loss of ordered stacking. In contrast, rU_{30} displays only weak helicity even at 0 °C, and its OCFs decay monotonically at all temperatures, suggesting that uracil-rich sequences respond more weakly to thermal perturbation (Fig. 4D). Compared with their corresponding dinucleotides, both rA_{30} and rU_{30} unstack more rapidly upon heating (Fig. 4E). Structural ensembles[117] of rA_{30} highlight drastic changes across temperatures: stacked and compact conformations dominate at low temperatures, expanded intermediates emerge at moderate temperatures, whereas collapsed structures prevail at high temperatures (Fig. 4F).

Reorganization of the Ion Atmosphere at Elevated Temperature. Across all conditions, Γ_{Mg} increases linearly with temperature (Fig. 5A), indicating enhanced Mg^{2+} absorption into the RNA ion atmosphere at elevated temperatures. It is consistent with the strengthening of electrostatic interactions as the dielectric constant of water decreases with temperature. Strikingly, our simulations unveil a clear redistribution of Mg^{2+} from the diffusive to the inner-sphere populations as temperature rises, while the outer-sphere contribution remains largely unchanged (Fig. 5B). Quantitatively, the number of inner-sphere ions increases by nearly 1.5 per RNA, accompanied by a corresponding decrease of about 1 ion in the diffusive population. At elevated temperatures, the inner-sphere ions outnumber the diffusive counterparts, signaling a temperature-driven collapse of the Mg^{2+} atmosphere surrounding the RNA. 2D ion density maps comparing between 0 °C and 100 °C

vividly illustrate this rearrangement. For rA_{30}, the diffusive layer becomes markedly depleted as ions migrate inward to form direct, inner-sphere contacts with phosphate groups. The concurrent loss of base stacking further accentuates this redistribution. rU_{30} also exhibits a similar shift (Fig. 5C), but the magnitude is much less pronounced, consistent with its weaker stacking propensity (Fig. 5D). This temperature-driven transition therefore reflects an entropically favored reorganization of the ion atmosphere. Formation of inner-sphere contacts requires partial dehydration of $Mg(H_2O)_6{}^{2+}$, an energetically costly process that releases tightly bound water molecules into bulk solvent. The resulting gain in translational and rotational entropy of released water grows with temperature, progressively offsetting the dehydration enthalpy and thus stabilizing direct Mg^{2+}–phosphate coordination. A similar finding has been reported for polyphosphates.[50]

Our findings provide a molecular explanation for how RNAs remain compact and functional at high temperature, especially in thermophilic organisms. In such environments, the strengthening of ion–phosphate interactions and the entropic benefit of dehydration act as intrinsic stabilizing mechanisms that compensate for the thermal weakening of base stacking and pairing. Enhanced ion coordination effectively "locks" the phosphate backbone and reduces electrostatic repulsion, maintaining RNA integrity at high temperatures. This mechanism complements sequence-level adaptations (such as higher G-C or purine content, and increased tertiary contacts) that have been documented in thermophilic ribozymes and ribosomal RNAs.[118–121] The temperature dependence of dielectric screening and hydration entropy thus emerges as an underappreciated factor in RNA thermostability and evolution. At the opposite extreme, our results also shed light on the physical basis of cold-induced RNA misfolding transitions.[122] At low temperature, water is highly structured and its dielectric constant is large, resulting in strong screening and reduced ion binding. This picture aligns with experimental observations of "cold denaturation" in nucleic acids, where enhanced hydration destabilizes compact structures.

The coupling between temperature-dependent base stacking and electrostatic conden-

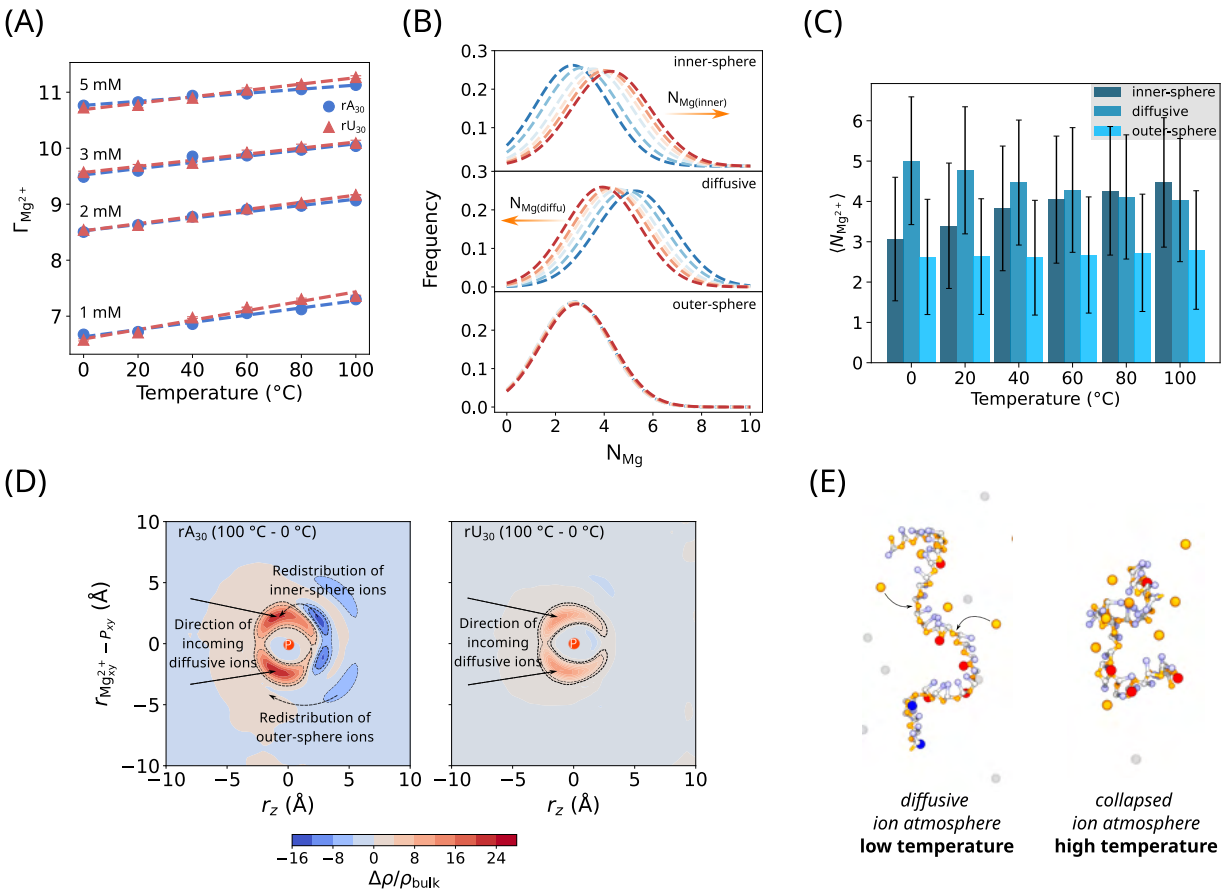

Figure 5: Ion reorganization at high temperature. **(A)** Preferential interaction coefficient for Mg^{2+} increases linearly with temperature for both rA_{30} (blue) and rU_{30} (red) at all Mg^{2+} concentrations. **(B)** Partitioning of rA_{30} ion atmosphere into inner-sphere (top), diffusive (middle), and outer-sphere (bottom) bindings. Increasing temperature drives ions from the diffusive to the inner-sphere regions. **(C)** Ion atmosphere composition from 0 to 100 °C of rU_{30} in 5 mM Mg^{2+}. **(D)** Difference in 2D ion density map (100 °C - 0 °C). **Left:** rA_{30} shows heating reorganizes diffusive ions towards inner-sphere binding, while outer-sphere and inner-sphere ions shift with the loss of stacking. **Right:** Reorganization is much weaker for rU_{30} than in rA_{30} due to smaller changes of stacking during heating. **(E)** Schematic illustration of diffusive-to-inner-sphere ion migration underlying temperature-induced collapse of the ion atmosphere.

sation also has implications for RNA condensates. Recent experiments have shown that RNA can undergo lower critical solution temperature(LCST)-type phase separation in the presence of Mg^{2+}.[50] Such LCST behavior is typically linked to a strong coupling between the single chain coil-to-globule transition and the driving force for phase separation.[123–125] The expansion of RNA at low temperature and its collapse at high temperature observed in this work are characteristic features of systems exhibiting LCST-type thermoresponsive behavior. Accordingly, our framework could provide a microscopic basis for interpreting RNA

LCST-type phase separation.

Conclusion

Our work establishes a molecular framework for understanding how temperature and ions together shape the structural ensemble of ssRNAs. Using CG simulations, we quantitatively reproduce experimental SAXS profiles (and R_g) accross a wide range of ion concentrations. Although ssRNAs are highly flexible and lack stable secondary structure, we show that base-stacking interactions govern the degree of right-handed helix formation, with rA_{30} forming the most persistent helical structure. Remarkably, while all sequences attract comparable numbers of ions, rU_{30} shows a slight preference for inner-sphere coordination, indicating sequence-dependent ion binding propensities. In contrast, the ion atmosphere around rA_{30} exhibits a small but detectable degree of chirality. These modest variations, though minor at the single-chain level, could enable binding partners to "sense" sequence identity through electrostatic or chiral recognition and are likely to be amplified in multichain contexts such as RNA condensate formation.

By incorporating a novel temperature-dependent Mg^{2+}-phosphate potential into the simulations, we are able to illustrate, for the first time, the interplay between RNA structural ensemble and its ion atmosphere across temperatures. Our simulations reveal a sequence-specific collapse of RNAs at high temperature due to differences in base-stacking propensity. Each sequence exhibits a non-monotonic compaction, with distinct expansion temperature maxima that shift downward in the presence of Mg^{2+}, underscoring the electrostatic origin of the transition. At high temperatures, transient helical structures are lost, rendering all sequences being equal. We show that Mg^{2+} binding increases linearly with temperature, consistent with the entropic nature of ion binding.[116,126] As temperature rises, ions migrate from diffuse to inner-sphere regions, directly linking RNA compaction to dehydration and tighter phosphate coordination. Together, these findings highlight that RNA ion atmosphere

is not passive screening layer but a dynamic, sequence-encoded extension of the RNA structure itself. By integrating counterion condensation, base stacking, and temperature-driven collapse within a unified framework, our study provides a molecular basis for understanding how simple RNA sequences undergo ion-mediated structural transitions and phase behaviors.

Acknowledgments

We thank Peter Eastman for valuable discussions regarding the implementation of simulations in OpenMM.

Author Contributions Statement

H.Z. implemented the model and the computational framework, analyzed the data, and took the lead in writing the manuscript. H.M. assisted with data analysis and model validation. H.T.N. supervised the project, guided data interpretation, and revised the manuscript.

Funding

We gratefully acknowledge financial support from the University at Buffalo to H.T.N.. Computational resources were provided by the Center for Computational Research at the University at Buffalo.

References

(1) Ding, Y.; Tang, Y.; Kwok, C. K.; Zhang, Y.; Bevilacqua, P. C.; Assmann, S. M. In vivo genome-wide profiling of RNA secondary structure reveals novel regulatory features. *Nature* **2014**, *505*, 696–700.

(2) Wan, Y.; Kertesz, M.; Spitale, R. C.; Segal, E.; Chang, H. Y. Understanding the transcriptome through RNA structure. *Nat. Rev. Genet.* **2011**, *12*, 641–655.

(3) Li, X.; Quon, G.; Lipshitz, H. D.; Morris, Q. Predicting in vivo binding sites of RNA-binding proteins using mRNA secondary structure. *RNA* **2010**, *16*, 1096.

(4) Garneau, N. L.; Wilusz, J.; Wilusz, C. J. The highways and byways of mRNA decay. *Nat. Rev. Mol. Cell. Biol.* **2007**, *8*, 113–126.

(5) Warf, M. B.; Berglund, J. A. Role of RNA structure in regulating pre-mRNA splicing. *Trends Biochem. Sci* **2010**, *35*, 169–178.

(6) Martin, K. C.; Ephrussi, A. mRNA Localization: Gene Expression in the Spatial Dimension. *Cell* **2009**, *136*, 719–730.

(7) Vicens, Q.; Kieft, J. S. Thoughts on how to think (and talk) about RNA structure. *Proc. Natl. Acad. Sci. U.S.A.* **2022**, *119*, e2112677119.

(8) Thirumalai, D.; Hyeon, C. RNA and Protein Folding: Common Themes and Variations. *Biochemistry* **2005**, *44*, 4957–4970.

(9) Bevilacqua, P. C.; Ritchey, L. E.; Su, Z.; Assmann, S. M. Genome-Wide Analysis of RNA Secondary Structure. *Annu. Rev. Genet.* **2016**, *50*, 235–266.

(10) Cech, T. R.; Bass, B. L. Biological catalysis by RNA. *Annu. Rev. Biochem.* **1986**, *55*, 599–629.

(11) Draper, D. E. A guide to ions and RNA structure. *RNA* **2004**, *10*, 335.

(12) Römer, R.; Hach, R. tRNA Conformation and Magnesium Binding. *Eur. J. Biochem.* **1975**, *55*, 271–284.

(13) Stein, A.; Crothers, D. M. Conformational changes of transfer RNA. The role of magnesium(II). *Biochemistry* **1976**, *15*, 160–168.

(14) Stein, A.; Crothers, D. M. Equilibrium binding of magnesium(II) by Escherichia coli tRNAfMet. *Biochemistry* **1976**, *15*, 157–160.

(15) Sanchez de Groot, N.; Armaos, A.; Graña-Montes, R.; Alriquet, M.; Calloni, G.; Vabulas, R. M.; Tartaglia, G. G. RNA structure drives interaction with proteins. *Nat. Commun.* **2019**, *10*, 3246.

(16) Ganser, L. R.; Kelly, M. L.; Herschlag, D.; Al-Hashimi, H. M. The roles of structural dynamics in the cellular functions of RNAs. *Nat. Rev. Mol. Cell. Biol.* **2019**, *20*, 474–489.

(17) Cantara, W. A.; Crain, P. F.; Rozenski, J.; McCloskey, J. A.; Harris, K. A.; Zhang, X.; Vendeix, F.

A. P.; Fabris, D.; Agris, P. F. The RNA modification database, RNAMDB: 2011 update. *Nucleic Acids Res.* **2011**, *39*, D195–D201.

(18) Delaunay, S.; Helm, M.; Frye, M. RNA modifications in physiology and disease: towards clinical applications. *Nat. Rev. Genet.* **2024**, *25*, 104–122.

(19) Cappannini, A.; Ray, A.; Purta, E.; Mukherjee, S.; Boccaletto, P.; Moafinejad, S. N.; Lechner, A.; Barchet, C.; Klaholz, B.; Stefaniak, F.; Bujnicki, J. M. MODOMICS: a database of RNA modifications and related information. 2023 update. *Nucleic Acids Res.* **2024**, *52*, D239–D244.

(20) Lewis, C. J. T.; Pan, T.; Kalsotra, A. RNA modifications and structures cooperate to guide RNA–protein interactions. *Nat. Rev. Mol. Cell. Biol.* **2017**, *18*, 202–210.

(21) Munroe, D.; Jacobson, A. mRNA Poly (A) Tail, a 3 Enhancer of Translational Initiation. *Mol. Cell. Biol.* **1990**, *10*, 3441–3455.

(22) Decker, C. J.; Parker, R. A turnover pathway for both stable and unstable mRNAs in yeast: evidence for a requirement for deadenylation. *Genes Dev.* **1993**, *7*, 1632–1643.

(23) Wang, Z.; Day, N.; Trifillis, P.; Kiledjian, M. An mRNA Stability Complex Functions with Poly(A)-Binding Protein To Stabilize mRNA In Vitro. *Mol. Cell. Biol.* **1999**, *19*, 4552–4560.

(24) Chen, Z.; Li, Y.; Krug, R. M. Influenza A virus NS1 protein targetspoly(A)-binding protein II of the cellular 3-end processing machinery. *EMBO J.* **1999**, *18*, 2273–2283.

(25) Tian, B.; Hu, J.; Zhang, H.; Lutz, C. S. A large-scale analysis of mRNA polyadenylation of human and mouse genes. *Nucleic Acids Res.* **2005**, *33*, 201–212.

(26) Craig, A. W. B.; Haghighat, A.; Yu, A. T. K.; Sonenberg, N. Interaction of polyadenylate-binding protein with the eIF4G homologue PAIP enhances translation. *Nature* **1998**, *392*, 520–523.

(27) Hall, T. M. T. Poly(A) tail synthesis and regulation: recent structural insights. *Curr. Opin. Struct. Biol.* **2002**, *12*, 82–88.

(28) Makeyev, A. V.; Liebhaber, S. A. The poly(C)-binding proteins: a multiplicity of functions and a search for mechanisms. *RNA* **2002**, *8*, 265.

(29) Eliseeva, I. A.; Lyabin, D. N.; Ovchinnikov, L. P. Poly(A)-binding proteins: Structure, domain organization, and activity regulation. *Biochemistry (Mosc)* **2013**, *78*, 1377–1391.

(30) Wigington, C. P.; Williams, K. R.; Meers, M. P.; Bassell, G. J.; Corbett, A. H. Poly(A) RNA-binding proteins and polyadenosine RNA: new members and novel functions. *WIREs RNA* **2014**, *5*, 601–622.

(31) Denman, R. B. Déjà vu all over again: FMRP binds U-rich target mRNAs. *Biochem. Biophys. Res. Commun.* **2003**, *310*, 1–7.

(32) Fresco, J. R.; Doty, P. Polynucleotides. I. Molecular Properties and Configurations OF Polyriboadenylic Acid in Solution. *J. Am. Chem. Soc.* **1957**, *79*, 3928–3929.

(33) Dewey, T. G.; Turner, D. H. Laser temperature-jump study of stacking in adenylic acid polymers. *Biochemistry* **1979**, *18*, 5757–5762.

(34) Leng, M.; Felsenfeld, G. A study of polyadenylic acid at neutral pH. *J. Mol. Biol.* **1966**, *15*, 455–466.

(35) Brahms, J. Optical activity and the conformation of polynucleotide models of nucleic acids. *J. Mol. Biol.* **1965**, *11*, 785–801.

(36) Adler, A. J.; Grossman, L.; Fasman, G. D. Polyriboadenylic and polydeoxyriboadenylic acids. Optical rotatory studies of pH-dependent conformations and their relative stability. *Biochemistry* **1969**, *8*, 3846–3859.

(37) Warshaw, M. M.; Bush, C.; Tinoco, I. The optical rotatory dispersion of adenylyl (3–5) adenosine and its significance for polynucleotide rotations. *Biochem. Biophys. Res. Commun.* **1965**, *18*, 633–638.

(38) Poland, D.; Vournakis, J. N.; Scheraga, H. A. Cooperative interactions in single-strand oligomers of adenylic acid. *Biopolymers* **1966**, *4*, 223–235.

(39) Brahms, J.; Mommaerts, W. F. H. M. A study of conformation of nucleic acids in solution by means of circular dichroism. *J. Mol. Biol.* **1964**, *10*, 73–88.

(40) Kondo, N. S.; Fang, K. N.; Miller, P. S.; Ts'o, P. O. Influence of the furanose on the conformation of adenine dinucleoside monophosphates in solution. *Biochemistry* **1972**, *11*, 1991–2003.

(41) Broido, M. S.; Kearns, D. R. Proton NMR evidence for a left-handed helical structure of poly(ribocytidylic acid) in neutral solution. *J. Am. Chem. Soc.* **1982**, *104*, 5207–5216.

(42) Holcomb, D. N.; Tinoco, I. Conformation of polyriboadenylic acid: pH and temperature dependence. *Biopolymers* **1965**, *3*, 121–133.

(43) Arnott, S.; Chandrasekaran, R.; Leslie, A. G. Structure of the single-stranded polyribonucleotide polycytidylic acid. *J. Mol. Biol.* **1976**, *106*, 735–748.

(44) Gellert, M.; Lipsett, M. N.; Davies, D. R. Helix formation by guanylic acid. *Proc. Natl. Acad. Sci. U.S.A.* **1962**, *48*, 2013–2018.

(45) Pörschke, D. The mode of Mg++ binding to oligonucleotides. Inner sphere complexes as markers for recognition? *Nucleic Acids Res.* **1979**, *6*, 883–898.

(46) Draper, D. E. RNA Folding: Thermodynamic and Molecular Descriptions of the Roles of Ions. *Biophys. J.* **2008**, *95*, 5489–5495.

(47) Hideki Aizaki, J. L. G. Nanoimaging of ssRNA: Genome Architecture of the Hepatitis C Virus Revealed by Atomic Force Microscopy. *J. Nanomed. Nanotechol.* **2011**, *s5*.

(48) Plumridge, A.; Meisburger, S. P.; Pollack, L. Visualizing single-stranded nucleic acids in solution. *Nucleic Acids Res.* **2017**, *45*, e66.

(49) Plumridge, A.; Andresen, K.; Pollack, L. Visualizing Disordered Single-Stranded RNA: Connecting Sequence, Structure, and Electrostatics. *J. Am. Chem. Soc.* **2020**, *142*, 109–119.

(50) Wadsworth, G. M.; Zahurancik, W. J.; Zeng, X.; Pullara, P.; Lai, L. B.; Sidharthan, V.; Pappu, R. V.; Gopalan, V.; Banerjee, P. R. RNAs undergo phase transitions with lower critical solution temperatures. *Nat. Chem.* **2023**, *15*, 1693–1704.

(51) Aumiller, W. M.; Keating, C. D. Phosphorylation-mediated RNA/peptide complex coacervation as a model for intracellular liquid organelles. *Nat. Chem.* **2016**, *8*, 129–137.

(52) Van Treeck, B.; Protter, D. S. W.; Matheny, T.; Khong, A.; Link, C. D.; Parker, R. RNA self-assembly contributes to stress granule formation and defining the stress granule transcriptome. *Proc. Natl. Acad. Sci.* **2018**, *115*, 2734–2739.

(53) Boeynaems, S.; Holehouse, A. S.; Weinhardt, V.; Kovacs, D.; Van Lindt, J.; Larabell, C.; Van Den Bosch, L.; Das, R.; Tompa, P. S.; Pappu, R. V.; Gitler, A. D. Spontaneous driving forces give rise to protein-RNA condensates with coexisting phases and complex material properties. *Proc. Natl. Acad. Sci.* **2019**, *116*, 7889–7898.

(54) Wang, T.; Hu, Q.; Fronhofer, S.; Pollack, L. Nucleotide-Specific RNA Conformations and Dynamics as Precursors to Ribonucleoprotein Condensates. *J. Am. Chem. Soc.* **2025**, *147*, 36146–36161.

(55) Tom, J. K. A.; Onuchic, P. L.; Deniz, A. A. Short PolyA RNA Homopolymers Undergo Mg2+-Mediated Kinetically Arrested Condensation. *J. Phys. Chem. B* **2022**, *126*, 9715–9725.

(56) Zgarbová, M.; Otyepka, M.; Šponer, J.; Mládek, A.; Banáš, P.; Cheatham, T. E. I.; Jurečka, P. Refinement of the Cornell et al. Nucleic Acids Force Field Based on Reference Quantum Chemical Calculations of Glycosidic Torsion Profiles. *J. Chem. Theory Comput.* **2011**, *7*, 2886–2902.

(57) Tubbs, J. D.; Condon, D. E.; Kennedy, S. D.; Hauser, M.; Bevilacqua, P. C.; Turner, D. H. The Nuclear Magnetic Resonance of CCCC RNA Reveals a Right-Handed Helix, and Revised Parameters for AMBER Force Field Torsions Improve Structural Predictions from Molecular Dynamics. *Biochemistry* **2013**, *52*, 996–1010.

(58) Condon, D. E.; Kennedy, S. D.; Mort, B. C.; Kierzek, R.; Yildirim, I.; Turner, D. H. Stacking in RNA: NMR of Four Tetramers Benchmark Molecular Dynamics. *J. Chem. Theory Comput.* **2015**, *11*, 2729–2742.

(59) Schrodt, M. V.; Andrews, C. T.; Elcock, A. H. Large-Scale Analysis of 48 DNA and 48 RNA Tetranucleotides Studied by 1 s Explicit-Solvent Molecular Dynamics Simulations. *J. Chem. Theory Comput.* **2015**, *11*, 5906–5917.

(60) Bergonzo, C.; Henriksen, N. M.; Roe, D. R.; Cheatham, T. E. Highly sampled tetranucleotide and tetraloop motifs enable evaluation of common RNA force fields. *RNA* **2015**, *21*, 1578–1590.

(61) Mlýnský, V.; Kührová, P.; Pykal, M.; Krepl, M.; Stadlbauer, P.; Otyepka, M.; Banáš, P.; Šponer, J. Can We Ever Develop an Ideal RNA Force Field? Lessons Learned from Simulations of the UUCG RNA Tetraloop and Other Systems. *J. Chem. Theory Comput.* **2025**, *21*, 4183–4202.

(62) Zhang, C.; Lu, C.; Jing, Z.; Wu, C.; Piquemal, J.-P.; Ponder, J. W.; Ren, P. AMOEBA Polarizable Atomic Multipole Force Field for Nucleic Acids. *J. Chem. Theory Comput.* **2018**, *14*, 2084–2108.

(63) Tan, D.; Piana, S.; Dirks, R. M.; Shaw, D. E. RNA force field with accuracy comparable to state-of-the-art protein force fields. *Proc. Natl. Acad. Sci. U.S.A.* **2018**, *115*, E1346–E1355.

(64) Boniecki, M. J.; Lach, G.; Dawson, W. K.; Tomala, K.; Lukasz, P.; Soltysinski, T.; Rother, K. M.; Bujnicki, J. M. SimRNA: a coarse-grained method for RNA folding simulations and 3D structure prediction. *Nucleic Acids Res.* **2016**, *44*, e63.

(65) Thirumalai, D.; Hori, N.; Nguyen, H. T. Minimal models for RNA simulations. *Curr. Opin. Struct. Biol.* **2025**, *93*, 103107.

(66) Šulc, P.; Romano, F.; Ouldridge, T. E.; Doye, J. P. K.; Louis, A. A. A nucleotide-level coarse-grained model of RNA. *J. Chem. Phys.* **2014**, *140*, 235102.

(67) Li, J.; Zhang, S.; Zhang, D.; Chen, S.-J. Vfold-Pipeline: a web server for RNA 3D structure prediction from sequences. *Bioinformatics* **2022**, *38*, 4042–4043.

(68) Uusitalo, J. J.; Ingólfsson, H. I.; Marrink, S. J.; Faustino, I. Martini Coarse-Grained Force Field: Extension to RNA. *Biophys. J.* **2017**, *113*, 246–256.

(69) Yasuda, I.; von Bülow, S.; Tesei, G.; Yamamoto, E.; Yasuoka, K.; Lindorff-Larsen, K. Coarse-Grained Model of Disordered RNA for Simulations of Biomolecular Condensates. *J. Chem. Theory Comput.* **2025**, *21*, 2766–2779.

(70) Li, S.; Chen, J. Driving Forces of RNA Condensation Revealed through Coarse-Grained Modeling with Explicit Mg2+. 2025; `https://www.biorxiv.org/content/10.1101/2024.11.17.624048v2`.

(71) Joseph, J. A.; Reinhardt, A.; Aguirre, A.; Chew, P. Y.; Russell, K. O.; Espinosa, J. R.; Garaizar, A.; Collepardo-Guevara, R. Physics-driven coarse-grained model for biomolecular phase separation with near-quantitative accuracy. *Nat. Comput. Sci.* **2021**, *1*, 732–743.

(72) Nguyen, H. T.; Hori, N.; Thirumalai, D. Condensates in RNA repeat sequences are heterogeneously organized and exhibit reptation dynamics. *Nat. Chem.* **2022**, *14*, 775–785.

(73) Maity, H.; Zhang, H.; Thirumalai, D.; Nguyen, H. T. RNA Structural Complexity Dictates Its Ion Atmosphere. *J. Phys. Chem. Lett.* **2025**, 8393–8402.

(74) Nguyen, H. T.; Hori, N.; Thirumalai, D. Theory and simulations for RNA folding in mixtures of monovalent and divalent cations. *Proc. Natl. Acad. Sci. U.S.A.* **2019**, *116*, 21022–21030.

(75) Chandler, D.; Andersen, H. C. Optimized Cluster Expansions for Classical Fluids. II. Theory of Molecular Liquids. *J. Chem. Phys.* **1972**, *57*, 1930–1937.

(76) Hirata, F.; Rossky, P. J. An extended rism equation for molecular polar fluids. *Chem. Phys. Lett.* **1981**, *83*, 329–334.

(77) Luchko, T.; Gusarov, S.; Roe, D. R.; Simmerling, C.; Case, D. A.; Tuszynski, J.; Kovalenko, A. Three-Dimensional Molecular Theory of Solvation Coupled with Molecular Dynamics in Amber. *J. Chem. Theory Comput.* **2010**, *6*, 607–624.

(78) Luchko, T.; Joung, I. S.; Case, D. A. In *Innovations in Biomolecular Modeling and Simulations*; Schlick, T., Schlick, T., Eds.; The Royal Society of Chemistry, 2012; Vol. 1; pp 51–86.

(79) Kast, S. M.; Kloss, T. Closed-form expressions of the chemical potential for integral equation closures with certain bridge functions. *J. Chem. Phys.* **2008**, *129*, 236101.

(80) Kovalenko, A.; Hirata, F. Self-consistent description of a metal–water interface by the Kohn–Sham density functional theory and the three-dimensional reference interaction site model. *J. Chem. Phys.* **1999**, *110*, 10095–10112.

(81) Perkyns, J.; Pettitt, B. M. A site–site theory for finite concentration saline solutions. *J. Chem. Phys.* **1992**, *97*, 7656–7666.

(82) Joung, I. S.; Luchko, T.; Case, D. A. Simple electrolyte solutions: Comparison of DRISM and molecular dynamics results for alkali halide solutions. *J. Chem. Phys.* **2013**, *138*, 044103.

(83) Denesyuk, N. A.; Thirumalai, D. Coarse-Grained Model for Predicting RNA Folding Thermodynamics. *J. Phys. Chem. B* **2013**, *117*, 4901–4911.

(84) Weeks, J. D.; Chandler, D.; Andersen, H. C. Role of Repulsive Forces in Determining the Equilibrium Structure of Simple Liquids. *J. Chem. Phys.* **1971**, *54*, 5237–5247.

(85) Xia, T.; SantaLucia, J. J.; Burkard, M. E.; Kierzek, R.; Schroeder, S. J.; Jiao, X.; Cox, C.; Turner, D. H. Thermodynamic Parameters for an Expanded Nearest-Neighbor Model for Formation of RNA Duplexes with Watson-Crick Base Pairs. *Biochemistry* **1998**, *37*, 14719–14735.

(86) Oosawa, F. *Polyelectrolytes*; M. Dekker, 1971.

(87) Manning, G. S. The molecular theory of polyelectrolyte solutions with applications to the electrostatic properties of polynucleotides. *Q. Rev. Biophys.* **1978**, *11*, 179–246.

(88) Record, M. T. J.; Anderson, C. F.; Lohman, T. M. Thermodynamic analysis of ion effects on the binding and conformational equilibria of proteins and nucleic acids: the roles of ion association or release, screening, and ion effects on water activity. *Q. Rev. Biophys.* **1978**, *11*, 103–178.

(89) Eastman, P. et al. OpenMM 8: Molecular Dynamics Simulation with Machine Learning Potentials. *J. Phys. Chem. B* **2024**, *128*, 109–116.

(90) Lipfert, J.; Doniach, S.; Das, R.; Herschlag, D. Understanding Nucleic Acid–Ion Interactions. *Annu. Rev. Biochem.* **2014**, *83*, 813–841.

(91) Kirkwood, J. G.; Buff, F. P. The Statistical Mechanical Theory of Solutions. I. *J. Chem. Phys.* **1951**, *19*, 774–777.

(92) Perry, Z. R.; Pyle, A. M.; Zhang, C. Arena: Rapid and Accurate Reconstruction of Full Atomic RNA Structures From Coarse-grained Models. *J. Mol. Biol.* **2023**, *435*, 168210.

(93) Pérez, A.; Marchán, I.; Svozil, D.; Sponer, J.; Cheatham, T. E.; Laughton, C. A.; Orozco, M. Refinement of the AMBER Force Field for Nucleic Acids: Improving the Description of / Conformers. *Biophys. J.* **2007**, *92*, 3817–3829.

(94) Svergun, D.; Barberato, C.; Koch, M. H. J. CRYSOL– a Program to Evaluate X-ray Solution Scattering of Biological Macromolecules from Atomic Coordinates. *J. Appl. Crystallogr.* **1995**, *28*, 768–773.

(95) Lavery, R.; Maddocks, J. H.; Pasi, M.; Zakrzewska, K. Analyzing ion distributions around DNA. *Nucleic Acids Res.* **2014**, *42*, 8138.

(96) Mitternacht, S. FreeSASA: An open source C library for solvent accessible surface area calculations. 2016; `https://f1000research.com/articles/5-189`.

(97) Lee, B.; Richards, F. M. The interpretation of protein structures: Estimation of static accessibility. *J. Mol. Biol.* **1971**, *55*, 379–IN4.

(98) Maaten, L. v. d.; Hinton, G. Visualizing Data using t-SNE. *J. Mach. Learn. Res.* **2008**, *9*, 2579–2605.

(99) McInnes, L.; Healy, J.; Astels, S. hdbscan: Hierarchical density based clustering. *J. Open Source Softw.* **2017**, *2*, 205.

(100) Appadurai, R.; Koneru, J. K.; Bonomi, M.; Robustelli, P.; Srivastava, A. Clustering Heterogeneous Conformational Ensembles of Intrinsically Disordered Proteins with t-Distributed Stochastic Neighbor Embedding. *J. Chem. Theory Comput.* **2023**, *19*, 4711–4727.

(101) Newby Lambert, M.; Vöcker, E.; Blumberg, S.; Redemann, S.; Gajraj, A.; Meiners, J.-C.; Walter, N. G. Mg^{2+}-Induced Compaction of Single RNA Molecules Monitored by Tethered Particle Microscopy. *Biophys. J.* **2006**, *90*, 3672–3685.

(102) Cantor, C. R.; Schimmel, P. R. *Biophysical chemistry*; Their Biophysical chemistry; W.H. Freeman: San Francisco, 1980.

(103) Bloomfield, V. A.; Crothers, D. M.; Tinoco, I. *Nucleic acids : structures, properties, and functions*; University Science Books: Sausalito, Calif, 2000.

(104) Seol, Y.; Skinner, G. M.; Visscher, K.; Buhot, A.; Halperin, A. Stretching of Homopolymeric RNA Reveals Single-Stranded Helices and Base-Stacking. *Phys. Rev. Lett.* **2007**, *98*, 158103.

(105) Saenger, W. *Principles of nucleic acid structure*; Springer advanced texts in chemistry; Springer-Verlag: New York, 1984.

(106) Spitale, R. C.; Incarnato, D. Probing the dynamic RNA structurome and its functions. *Nat. Rev. Genet.* **2023**, *24*, 178–196.

(107) Strobel, E. J.; Yu, A. M.; Lucks, J. B. High-throughput determination of RNA structures. *Nat. Rev. Genet.* **2018**, *19*, 615–634.

(108) Jacobson, D. R.; Saleh, O. A. Counting the ions surrounding nucleic acids. *Nucleic Acids Res.* **2017**, *45*, 1596–1605.

(109) Mondal, B.; Chakraborty, D.; Hori, N.; Nguyen, H. T.; Thirumalai, D. Competition between Stacking and Divalent Cation-Mediated Electrostatic Interactions Determines the Conformations of Short DNA Sequences. *J. Chem. Theory Comput.* **2024**, *20*, 2934–2946.

(110) Nguyen, H. T.; Thirumalai, D. Charge Density of Cation Determines Inner versus Outer Shell Coordination to Phosphate in RNA. *J. Phys. Chem. B* **2020**, *124*, 4114–4122.

(111) McDermott, M. L.; Vanselous, H.; Corcelli, S. A.; Petersen, P. B. DNA's Chiral Spine of Hydration. *ACS Cent. Sci.* **2017**, *3*, 708–714.

(112) Young, M. A.; Ravishanker, G.; Beveridge, D. L. A 5-nanosecond molecular dynamics trajectory for B-DNA: analysis of structure, motions, and solvation. *Biophys. J.* **1997**, *73*, 2313–2336.

(113) Liepinsh, E.; Otting, G.; Wüthrich, K. NMR observation of individual molecules of hydration water bound to DNA duplexes: direct evidence for a spine of hydration water present in aqueous solution. *Nucleic Acids Res.* **1992**, *20*, 6549–6553.

(114) Kopka, M. L.; Fratini, A. V.; Drew, H. R.; Dickerson, R. E. Ordered water structure around a B-DNA dodecamer. A quantitative study. *J. Mol. Biol.* **1983**, *163*, 129–146.

(115) Hori, N.; Denesyuk, N. A.; Thirumalai, D. Ion Condensation onto Ribozyme Is Site Specific and Fold Dependent. *Biophys. J.* **2019**, *116*, 2400–2410.

(116) Chen, S.; Wang, Z.-G. Driving force and pathway in polyelectrolyte complex coacervation. *Proc. Natl. Acad. Sci. U.S.A.* **2022**, *119*, e2209975119.

(117) Wang, T.; Coshic, K.; Badiee, M.; McDonald, M. R.; Aksimentiev, A.; Pollack, L.; Leung, A. K. L. Cation-induced intramolecular coil-to-globule transition in poly(ADP-ribose). *Nat. Commun.* **2024**, *15*, 7901.

(118) Fang, X.-W.; Golden, B. L.; Littrell, K.; Shelton, V.; Thiyagarajan, P.; Pan, T.; Sosnick, T. R. The thermodynamic origin of the stability of a thermophilic ribozyme. *Proc. Natl. Acad. Sci. U.S.A.* **2001**, *98*, 4355–4360.

(119) Hu, E.-Z.; Lan, X.-R.; Liu, Z.-L.; Gao, J.; Niu, D.-K. A positive correlation between GC content and growth temperature in prokaryotes. *BMC Genomics* **2022**, *23*, 110.

(120) Nissley, A. J.; Penev, P. I.; Watson, Z. L.; Banfield, J. F.; Cate, J. H. D. Rare ribosomal RNA sequences from archaea stabilize the bacterial ribosome. *Nucleic Acids Res.* **2023**, *51*, 1880–1894.

(121) Becskei, A.; Rahaman, S. The life and death of RNA across temperatures. *Comput. Struct. Biotechnol. J.* **2022**, *20*, 4325–4336.

(122) Rissone, P.; Severino, A.; Pastor, I.; Ritort, F. Universal cold RNA phase transitions. *Proc. Natl. Acad. Sci. U.S.A.* **2024**, *121*, e2408313121.

(123) Lin, Y.-H.; Chan, H. S. Phase Separation and Single-Chain Compactness of Charged Disordered Proteins Are Strongly Correlated. *Biophys. J.* **2017**, *112*, 2043–2046.

(124) Dignon, G. L.; Zheng, W.; Best, R. B.; Kim, Y. C.; Mittal, J. Relation between single-molecule properties and phase behavior of intrinsically disordered proteins. *Proc. Natl. Acad. Sci. U.S.A.* **2018**, *115*, 9929–9934.

(125) Zeng, X.; Holehouse, A. S.; Chilkoti, A.; Mittag, T.; Pappu, R. V. Connecting Coil-to-Globule Transitions to Full Phase Diagrams for Intrinsically Disordered Proteins. *Biophys. J.* **2020**, *119*, 402–418.

(126) Ou, Z.; Muthukumar, M. Entropy and enthalpy of polyelectrolyte complexation: Langevin dynamics simulations. *J. Chem. Phys.* **2006**, *124*, 154902.

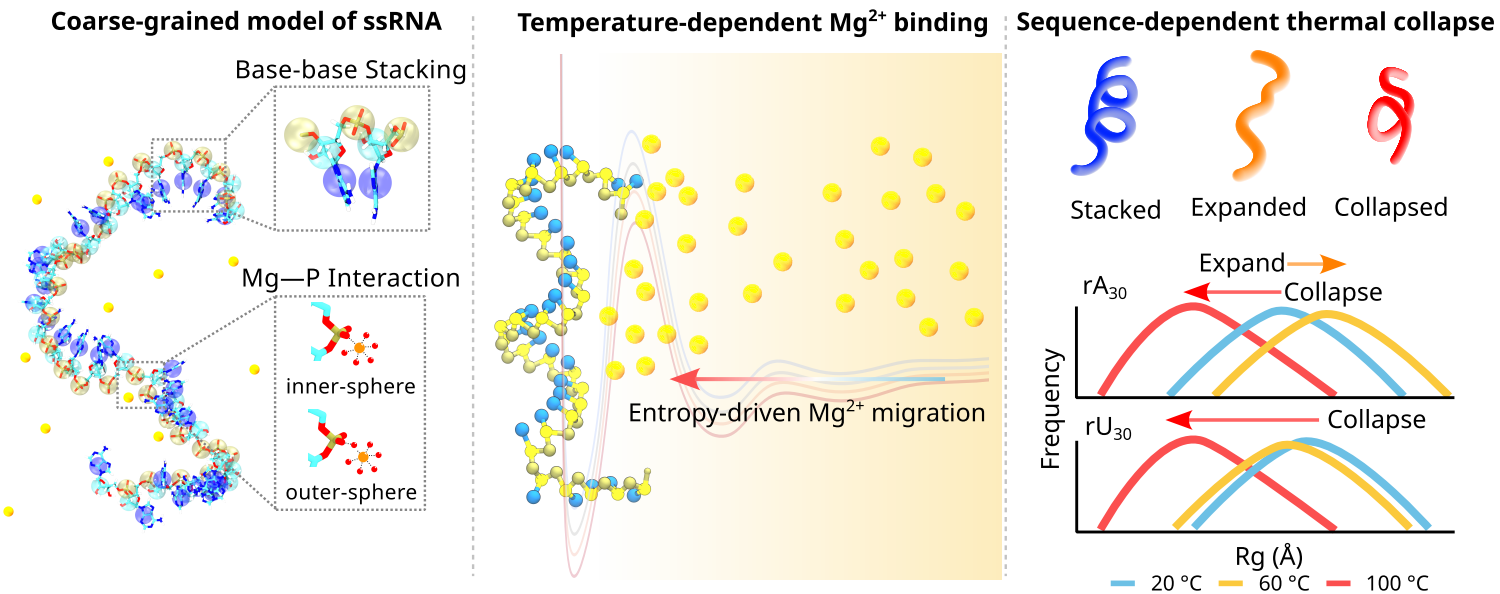
Coarse-grained model of ssRNA
Base-base Stacking
Mg—P Interaction
inner-sphere
outer-sphere
Temperature-dependent Mg2+ binding
Entropy-driven Mg2+ migration
Sequence-dependent thermal collapse
Stacked
Expanded
Collapsed
Expand
Collapse
rA30
rU30
Frequency
Rg (Å)
20 °C
60 °C
100 °C